Supplementary Materials for

Structure of the activated ROQ1 resistosome directly recognizing the pathogen effector XopQ

Raoul Martin*, Tiancong Qi*, Haibo Zhang, Furong Liu, Miles King, Claire Toth, Eva Nogales†, Brian J. Staskawicz†

*These authors contributed equally to this work.
†Corresponding author. Email: enogales@lbl.gov (E.N.); stask@berkeley.edu (B.J.S.)

This PDF file includes:

Materials and Methods
Supplementary Text
Figs. S1 to S13
Table S1
Caption for Movie S1
References

Other Supplementary Material for this manuscript includes the following:
(available at science.sciencemag.org/content/370/6521/eabd9993/suppl/DC1)

Movie S1 (mp4)
Sequence Alignment File S1 (PDF)
MDAR Reproducibility Checklist (PDF)

Materials and Methods

Plant Materials and Growth Conditions

The *N. benthamiana eds1-1* mutant was described as previously (14). The binary vector containing ROQ1 guide sequence (GATGATAAGGAGTTAAAGAG) and Cas9 was described previously (15) was transformed into agrobacterium and used for generating *N. tabacum roq1-1* stable mutant plants by CRISPR-Cas9 gene editing system. *N. benthamiana* and *N. tabacum* plants were grown in a growth chamber under a 8-hr-light/16-hr-dark photoperiod at 23-25℃.

Expression and Purification of the ROQ1-XopQ Complex

ROQ1 and XopQ were fused with C-terminal 3xFlag tag and N-terminal StrepII tag, respectively, and transformed into Agrobacterium GV3101. The agrobacterium GV3101 strains containing ROQ1-3xFlag and StrepII-XopQ were co-inoculated into *N. benthamiana eds1-1* mutant leaves. At 30 hours after infiltration, 200g of leaves were harvested and ground using a mortar and pestle and resuspended in 400 mL of Lysis Buffer (50 mM HEPES pH 7.5, 1 mM EDTA. 5 mM MgCl2, 150 mM NaCl, 10 mM KCl, 0.4% NP40, 5% glycerol, 10 mM DTT) supplemented with protease inhibitors (100 uM PMSF, 1 uM Phosphoramidon, 10 uM 1,10-Phenanthrolin, 1uM Pepstatin A, 10 uM Leupeptin, 2 uM E-64, 10 uM Bestatin and 2 ug/mL Aprotinin). Leaves were further lysed by sonication for 2 min at 20 kHz. The cell lysate was initially centrifuged at 18,000xg for 45 min to pellet large debris and the harvested supernatant was further centrifuged at 40,000xg for 45 min to remove any smaller residuals. The clarified extract was then incubated with 800 µL (bed volume) of ANTI-FLAG M2 affinity gel (Sigma-Aldrich) for 3 hours at 4℃. The gel was washed with 10 CV of Wash Buffer (20 mM HEPES pH 7.5, 1mM EDTA, 5 mM MgCl2, 150 mM NaCl, 10 mM KCl, 0.2% NP-40, 10% glycerol) and the sample was eluted twice by incubating in 1 CV of Wash Buffer supplemented with 300 µg/mL of 3xFlag peptide for 30 min. Each wash and elution was separated from the affinity-resin by centrifugation at 300xg for 5 min. Eluates were pooled and incubated with 20 µL (bed volume) of Strep-Tactin Superflow Plus (Qiagen) resin for 1 hour. The resin was then washed with 10 CV of Wash Buffer and the totality of the sample was eluted in 5 sequential steps by adding 1 CV Wash Buffer supplemented with 10 mM Biotin. Each wash and elution was separated from the affinity-resin by centrifugation at 300xg for 5 min. The protein complex was flash frozen in liquid N_2 and stored at -80˚C. Individual steps can be visualized by SDS-PAGE in Fig. S13. We were unable to accurately measure the final protein concentration due to low amounts of sample.

Sample Preparation for Cryo-EM

QUANTIFOIL R2/2 holey carbon grids were coated with a thin film of continuous carbon (approximately 3 nm thick) and plasma cleaned (Tergeo-EM, PIE Scientific LLC, operating at 15 W for 30 sec in indirect mode) before addition of sample. Because of the low concentration of the ROQ1-XopQ complex in our sample, we attempted to float the carbon-coated grid on the sample drop to enable prolonged incubation to allow attachment of more molecules to the carbon. However, due to the high detergent concentration of the sample buffer, loss of surface tension caused the grids to sink to the bottom of the drop. Therefore, we used a Teflon well to hold 20 µL of sample (supplemented with 1 mM ATP) and deposited the grid in the well carbon side up, upon which the grid fell to the bottom of the well, allowing sample adsorption to the carbon-coated side.

1

The grid was incubated with the sample for 90 min at 4℃. It was then removed from the drop and washed in a 50 µL drop of cryo-EM-friendly buffer (10 mM HEPES pH 7.5, 1 mM EDTA, 5 mM MgCl$_2$, 150 mM NaCl, 10 mM KCl, 3% trehalose). We gently blotted the grid using filter paper and added 4 µL of cryo-EM-friendly Buffer before mounting the grid onto a Thermo Fisher Scientific Vitrobot Mk. IV set to 100% humidity, cooled to 4℃ and loaded with Whatman Grade 1 Qualitative Filter Paper (GE Healthcare). The grid was immediately blotted for 10 sec (blot force 10) and plunge-frozen in liquid ethane.

Data Collection

The grid was loaded onto a Titan Krios cryo-electron microscope (Thermo Fisher Scientific) operating at 300 kV and equipped with a K3 direct electron detector camera (Gatan) mounted behind a BioQuantum energy filter (Gatan). Electron micrographs were acquired as dose-fractionated movies (11,134 movies in total) in super-resolution counting mode with the microscope set to 80,879x magnification (corresponding to a pixel size of 0.9386 Å) and a total electron exposure of 50 e$^-$/Å^2. Defocus values ranged from -0.9 to -2.5 µm. Automated data collection was controlled by SerialEM. For high-throughput data collection, we used image shift with active beam tilt correction enabled to collect 20 movies at each stage position. All other parameters can be found in Table S1.

Data Processing

All processing steps were performed using RELION 3.1(*43*) unless otherwise indicated. Movies were imported into RELION and classified into 5 optics groups according to the respective beam shift used during acquisition. Alignment of the movie frames was performed using MotionCor2(*45*) and GCTF(*44*) was used for fitting of the contrast transfer function and defocus estimation. To ensure that we captured particles in all poses present on the grid, we used the unbiased Laplacian-of-Gaussian autopicker(*50*) in RELION for particle picking. Instead of 2D classification, an initial 3D classification (with C4 symmetry applied) was performed in order to prevent loss of rare views that might be classified into classes containing broken particles or false-positive particle picks in 2D classification. An initial reconstruction of the ROQ1-XopQ complex generated in cryoSPARC(*51*) from a grid quality screening session was used as the reference model. The particles from the best classes in this initial 3D classification were subjected to successive rounds of alignment-free 3D classification, and alignment-free 2D classification for each 3D class, followed by removal of bad particles and 3D refinement. This enabled us to recover the side views of the ROQ1-XopQ complex, which we failed to do using alternative processing approaches. A final round of 3D-refinement and alignment-free 3D classification (tau = 16) yielded one high-quality class containing 15,263 particles, with a broad distribution of projection directions. After CTF-refinement and Bayesian polishing (*50*) of these particles, 3D-refinement resulted in a reconstruction of the ROQ1-XopQ complex at 3.8 Å resolution overall (FSC = 0.143). This initial map was of sufficient quality for atomic model building of the NB-ARC region (NBD-HD1-WHD) as well as the most N-terminal portion of the LRR. Further processing was needed to improve the LRR-PL-XopQ and TIR domain regions. To resolve the interaction between ROQ1 and XopQ, we applied symmetry expansion to our particles and performed a focused refinement using a mask around one LRR-PL-XopQ module. The angular search space was restricted to preserve the particle orientations after symmetry expansion. The resulting reconstruction converged to 3.8 Å resolution, displaying clear

separation between β-strand of the LRR and PL, as well as densities for the sidechains that interact with XopQ.

To improve the TIR domain map, we applied signal subtraction to our particles using a 3D mask around the TIR domains and selected particles exhibiting good density in this region by alignment-free 3D classification. This improved the overall signal for the TIR domain but the features of the density were too poor to confidently fit a model into this four-fold symmetric map. We reasoned that the poor map quality might originate from a symmetry mismatch between the TIR domains and the remainder of the complex, with the TIR domains possibly assuming lower symmetry. Therefore, we applied symmetry expansion to the particles subset and classified the data using alignment-free classification after signal subtraction to remove everything except the TIR domains from the particle images. The particles split equally into two identical classes rotated 90° relative to each other, revealing four TIR domains forming a dimer of dimers with C2 symmetry. Focused refinement of the TIR and NB-ARC regions (the signal from TIR domains alone was too small for proper particle alignment) improved the overall resolution to 4.6 Å, but the NB-ARC region is better resolved than the TIR domains. Based on local resolution estimation, the resolution of the TIR domains is around 7.5 Å, with the highest resolution features observed at the interface between the TIR domains. The onset of phase randomisation leads to an artifact in the corrected half-map FSC curve. For the graphical representation, we have removed three points of the FSC curves near 20 Å resolution to correct for this.

Model Building and Refinement
Each of the three cryo-EM maps (NB-ARC region, LRR-PL-XopQ module, and TIR domains) were used separately to build atomic models of the different parts of the ROQ1-XopQ complex. Initially, a model generated using SWISS-MODEL(*52*) based on the structure of ZAR1 NBD (PDB: 6J5T) was docked into our cryo-EM map using UCSF Chimera (*61*). This model served as a starting point to build the structure of the NB-ARC domain manually in COOT(*46*). Our initial map of the ROQ1-XopQ complex was used to build residues 189-625 of ROQ1 as well as for fitting the ATP ligand. The map resulting from the focused classification around the LRR-PL-XopQ region was then used to build the following C-terminal residues of ROQ1. We used the secondary-structure prediction algorithm in Phyre2(*53*) to guide us in building our model, specifically matching densities of β-strands and α-helices to sequences of residues with a corresponding predicted secondary structure. In a few cases, poorly resolved linker regions between β-strands were left unmodeled. We used the densities of large side chains and nearby secondary structure elements to ensure correct register assignment of the residues that followed. The structure of the open conformation of XopQ from *Xanthomonas oryzae pv. oryzae* (PDB: 4KL0) was used to fit XopQ into our density. The minor sequence differences with XopQ from *Xanthomonas euvesicatoria* were fixed in COOT(*46*).

A model for the ROQ1 TIR domain was generated in SWISS-MODEL(*52*) using the structure of the plant RPV1 TIR domain (PDB: 5KU7), as it shares the most sequence similarity among published structures. Four individual TIR domain monomers were docked in the TIR domain map using Chimera(*54*) and modified in COOT(*46*) to properly fit the density.

The atomic models for the TIR domain, the NB-ARC domain and LRR-PL-XopQ region were each refined in their respective maps with successive rounds of real-space refinement in PHENIX(*47*). Iterative rounds of rigid-body refinement, morphing and gradient driven global minimization were used in the initial stages of refinement while applying ramachandran, rotamer, $C_β$, and secondary structure restraints throughout to maintain good model geometry at

the resolution of our cryo-EM maps. Internal symmetry was imposed on the NB-ARC model and the TIR domain model. Structural issues were corrected manually in COOT(*46*) between rounds of refinement. The final model was refined using atomic displacement parameter refinement and gradient driven global minimization while applying the same restraint as described previously. The model was validated using MOLPROBITY(*55*) within PHENIX(*47*), and the model vs. map FSC was calculated using the MTRIAGE(*48*) validation tool in PHENIX(*47*).

HR Phenotype and Protein Expression
The various ROQ1 mutants were made and constructed into PE1776 vectors fusing with a C-terminal 3Flag tag. For HR phenotype observation, ROQ1 mutants and StrepII-XopQ were transiently co-expressed in *N. tabacum roq1-1* mutant leaves via agrobacterium mediated transformation. HR phenotypes were observed and imaged 2 days post infiltration. To detect protein expressions, ROQ1 mutants and StrepII-XopQ were co-expressed in *N. benthamiana eds1-1* mutant leaves, extracted using protein extraction buffer (50 mM Tris-HCl, pH 7.5, 150 mM NaCl, 1mM EDTA, 0.2% Nonidet P-40, 0.2%Triton X-100, 6 mM β-mercaptoethanol, 10mM DTT and 1×Protease Inhibitor Cocktail), boiled in Laemmli buffer for 5 min and separated on 8% SDS-PAGE gels. StrepII-XopQ were detected with the primary StrepTag II monoclonal antibody (A02230, Abbkine) and the second antibody (A4416, Sigma). ROQ1 mutants were enriched by ANTI-FLAG M2 Affinity Gel (A2220, Sigma-Aldrich) before boiled, and detected with the primary monoclonal anti-Flag antibody (F1804, Sigma-Aldrich) and the second antibody (A4416, Sigma).

Conservation of the Roq1 C-JID
The conservation scores for each residue in the C-JID of Roq1 (1129-1306) were calculated in Consurf (*52*). Unique homologous sequences with a sequence identity between 20% and 95% were collected from UNIREF90 using 3 iterations of the PSI-BLAST search algorithm (E-value: 0.0001). The 38 unique sequences found were aligned using MAFFT(*56*). In some regions, too few sequences aligned to calculate a reliable conservation score (positions occupied by fewer than 6 amino acids in the multiple sequence alignment are deemed to have unreliable scores) and were colored in gray. This occurred in our alignment at positions 1179-1200 (corresponding to a part of the NR loop of Roq1 that recognizes XopQ's active site) for which only 2 homologues found were aligned with. An alignment file is provided in the supplementary material (Sequence alignment file S1).
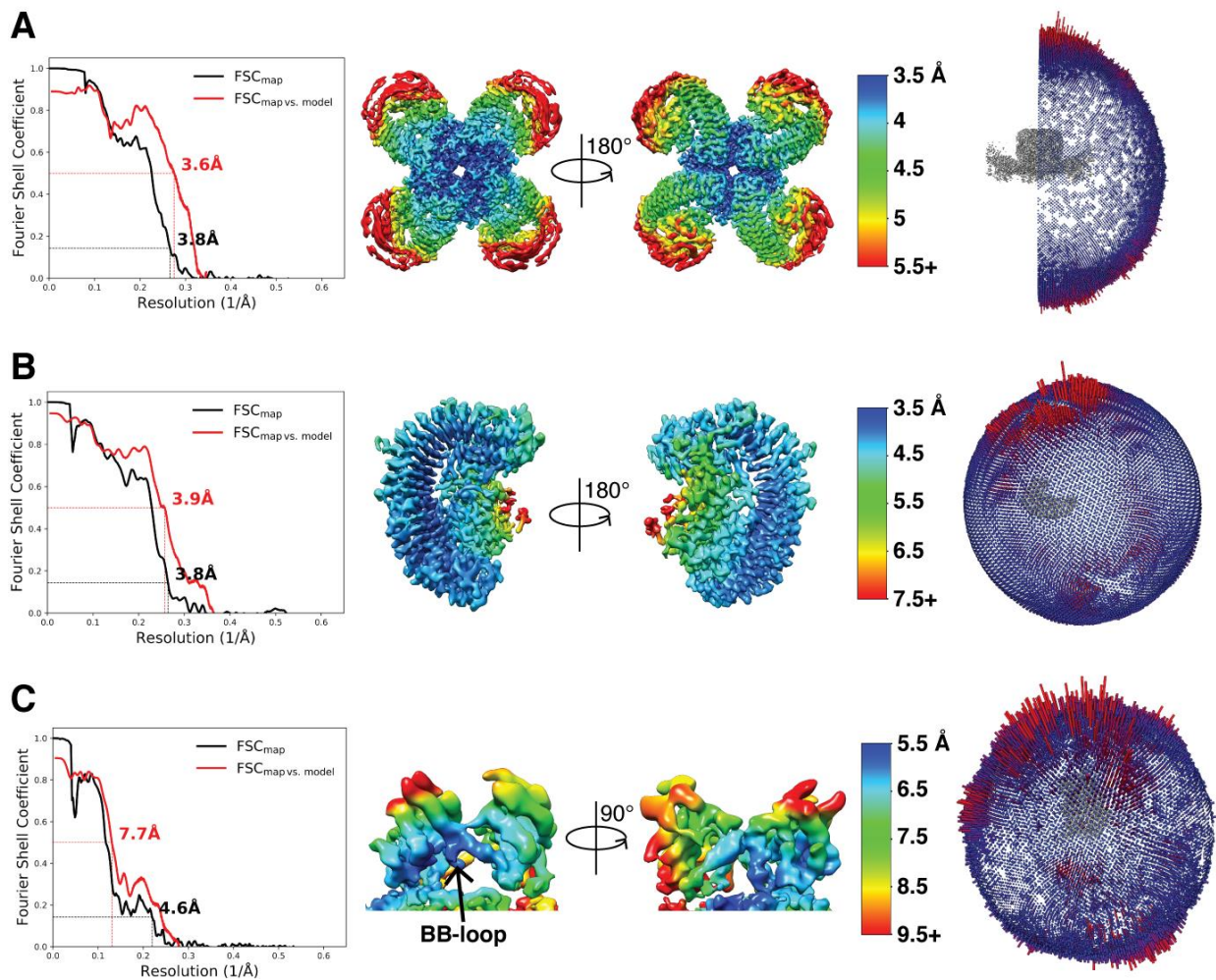
Fig. S1.

Resolution estimation. Left: map FSC and map vs model FSC for the three reconstructions used to build the atomic model of the ROQ1-XopQ complex. Right: Local resolution for each map. (A) Map vs model FSC calculated using residues 189-625 of ROQ1, corresponding to the NB-ARC and the N-terminal region of the LRR. (B) Map vs model FSC calculated using residues 526-1303 of ROQ1, corresponding to the LRR-PL region, and 89-453 of XopQ. (C) Map vs model FSC calculated using residues 11-176 of ROQ1, corresponding to the TIR domain.
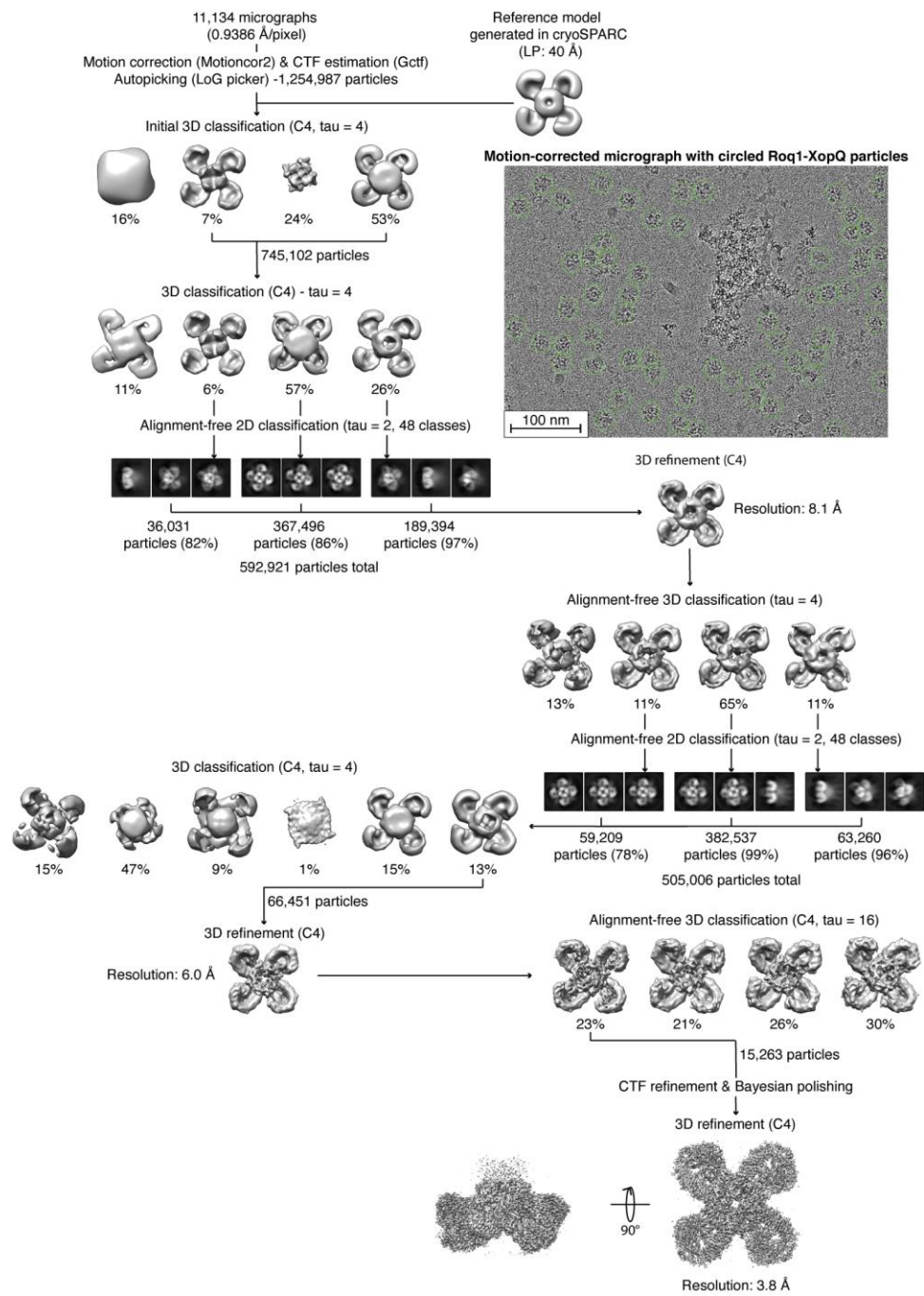
Fig. S2.

Cryo-EM data processing tree from collected EM movies to the initial reconstruction of the ROQ1-XopQ complex.
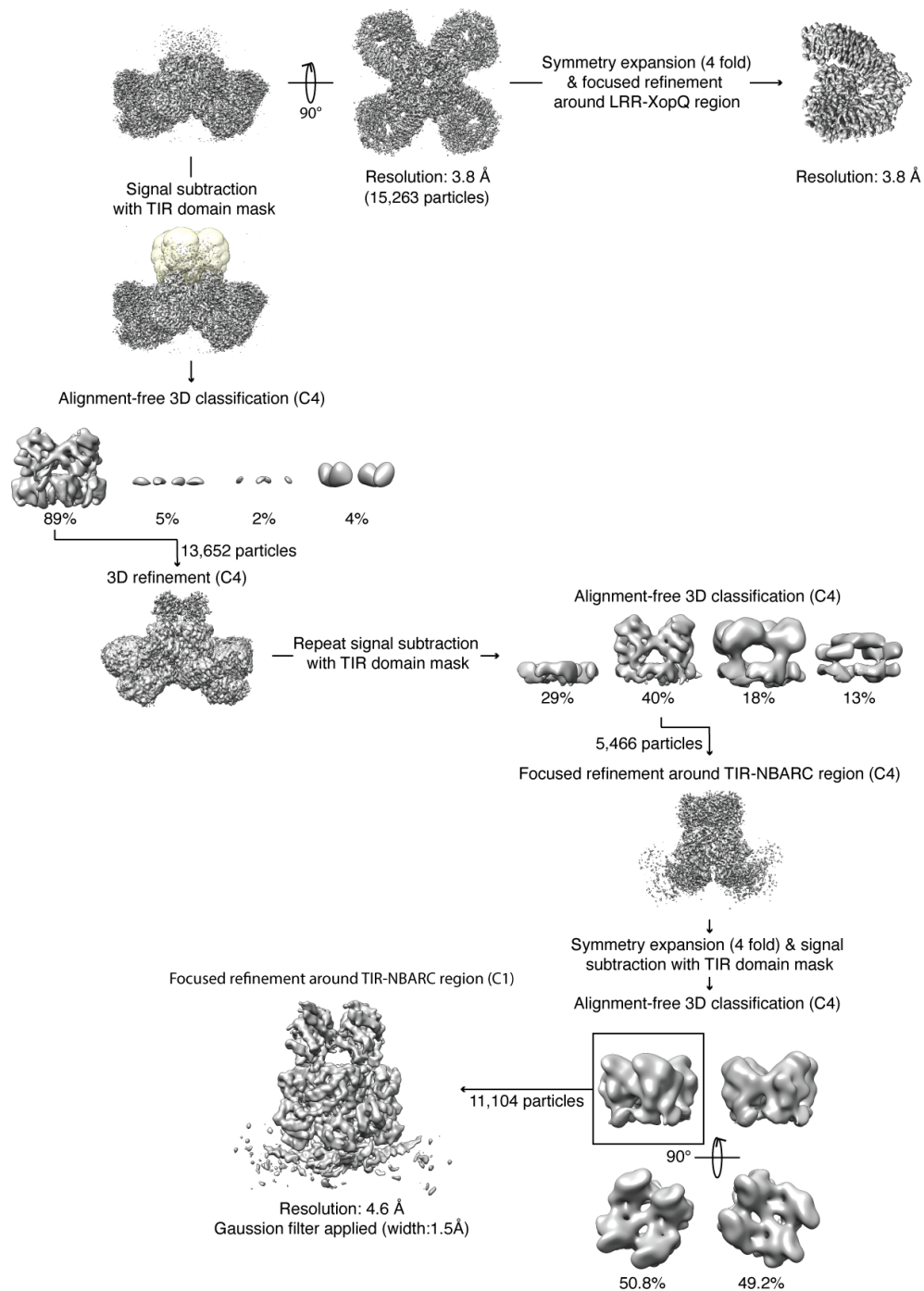
Fig. S3.

Further cryo-EM data processing needed to resolve the LRR-PL-XopQ region and the TIR

domains.
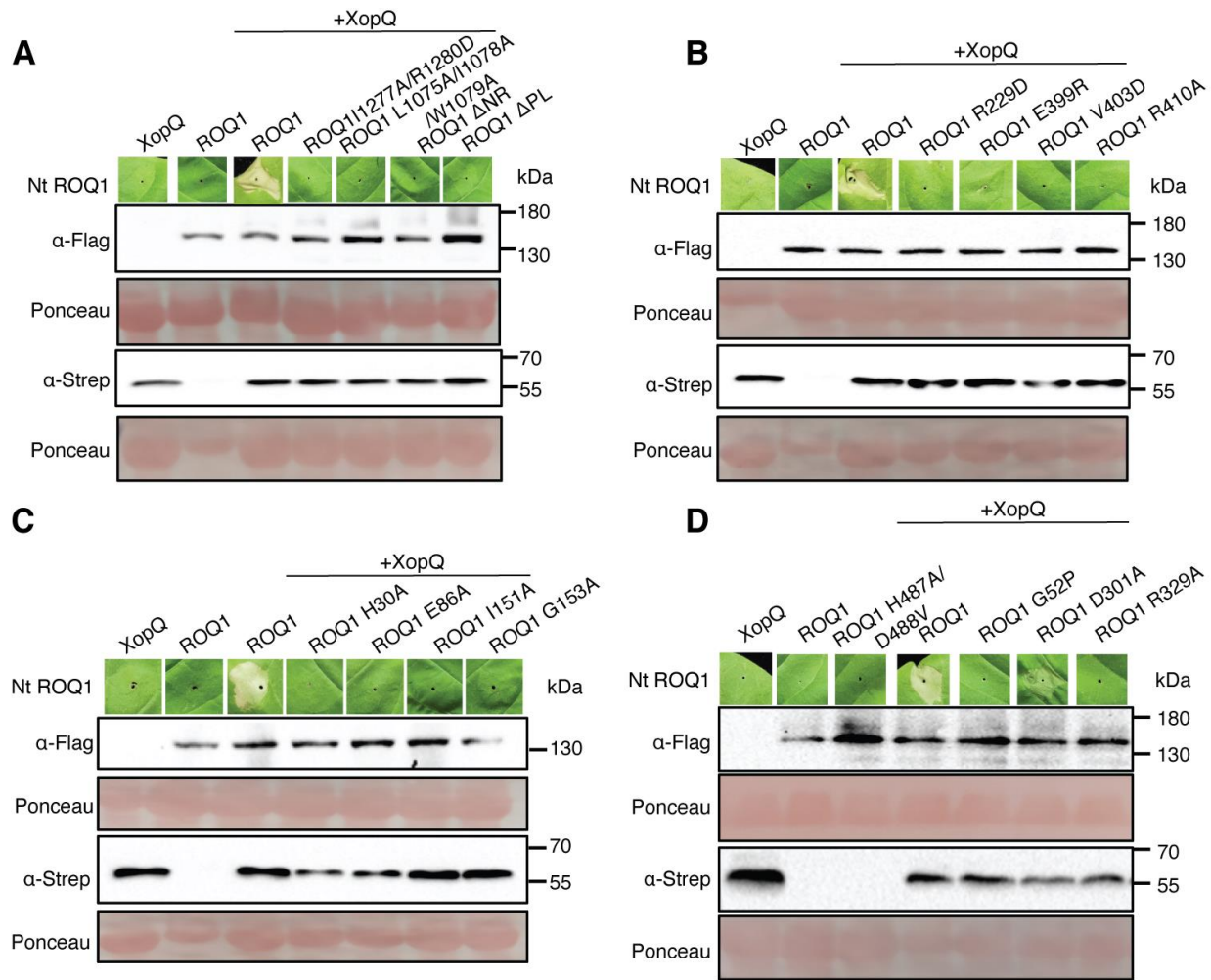
Fig. S4.

HR Phenotype and Protein Expression of ROQ1 mutants. The HR phenotype is detected on the leaf tissue at the site of agrobacterium injection (top row). Expression of ROQ1 and XopQ was detected by Western-blotting using an anti-Flag antibody and an anti-StrepTagII antibody respectively. Ponceau staining was used for the detection of protein bands on the Western-blots.

(A) Mutation in the LRR-PL-XopQ interface. Residues providing contacts between XopQ and the LRR (ROQ1 L1075A/I1078A/W1079A) as well between XopQ and the PL domain (ROQ1 I1277A/ R1280D, ΔNR and ΔPL) were mutated. For the ΔNR mutant, residues corresponding to the NR loop of Roq1 (1163-1195) were replaced with a flexible linker with the following

sequence: SGGGSGGS. For the ΔPL mutant, the C-terminal end of ROQ1 (1129-1306), corresponding to the PL domain, was truncated. (B) Mutations at the oligomerization interface of ROQ1 in the NB-ARC domain. More specifically, the R229 is at the NDB-NBD interface and E399, V403 and R410 are at the HD1-WHD interface. (C) Mutations in the TIR domain of ROQ1 at the AE (H30A) and BE (I151A, G153A) interfaces. The catalytic glutamate in the active site of the TIR domain (E86) was mutated to an alanine. (D) Additional mutations: in the MHD motif (H487A/D488V), the TIR domain BB-loop glycine (G52P), the Walker B motif (D301A) and the TTR motif (R329A).
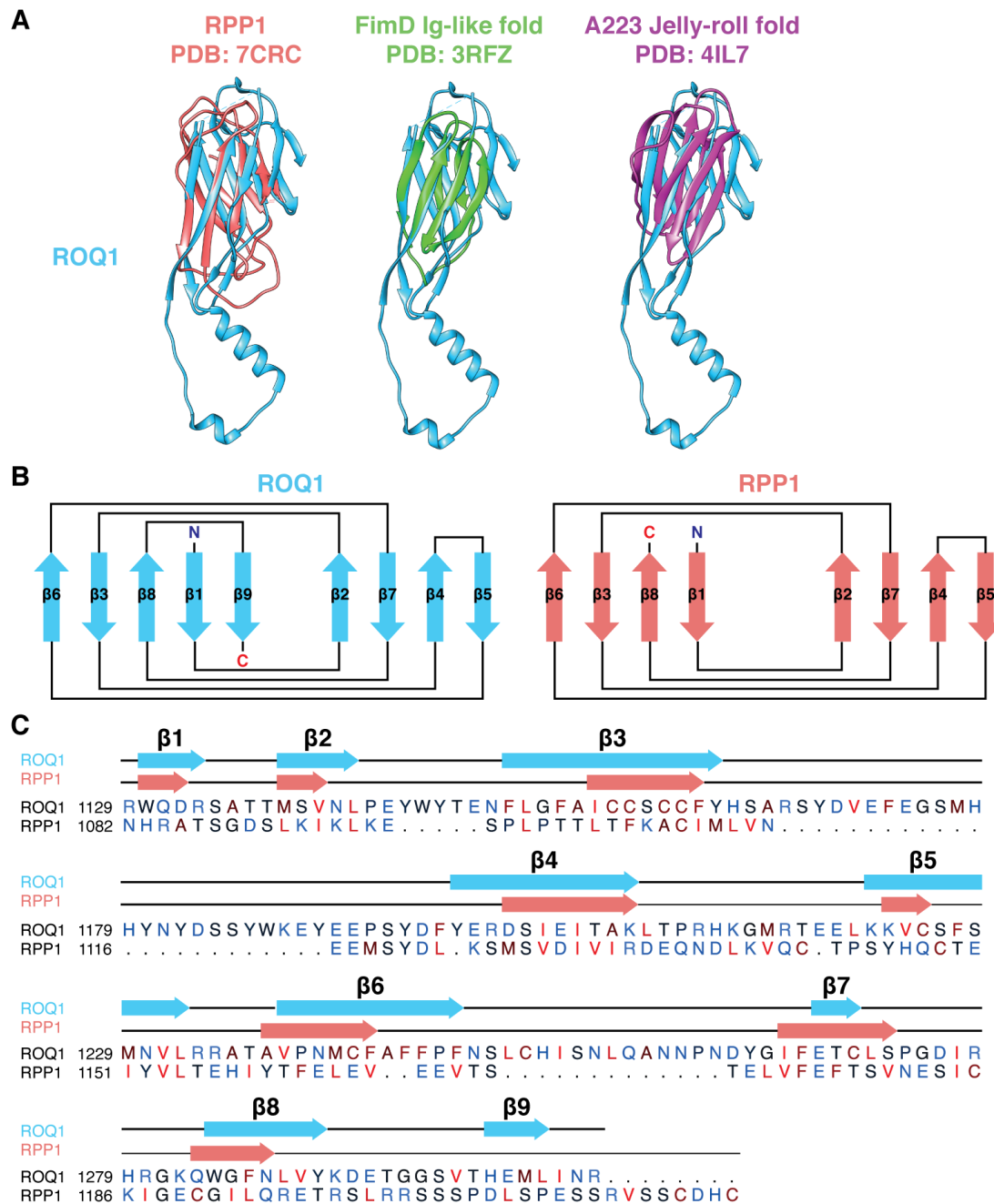
Fig. S5.

Comparison between the ROQ1 C-JID (PL domain) and the RPP1 C-JID. (A) From left to right: Structural alignment of the ROQ1 C-JID with the RPP1 C-JID (PDB: 7CRC), the Ig-like fold in FimD (PDB: 3RFZ), and the Jelly-roll fold in A223 (PDB: 4IL7). FimD and A223 were among

the highest scoring structural homologous of the ROQ1 C-JID found using the CATH database (*17*) and were used as representatives of their respective folds. (B) β-stand topology of ROQ1 (left) and RPP1 (right). The only difference found is at the 9th β-stand of ROQ1 which does not appear in the RPP1 structure. (C) Local sequence alignment between the ROQ1 C-JID (1129-1306) and the RPP1 C-JID (1082-1221). Positions of the β-stands in ROQ1 and RPP1 are labeled along the sequence using the same color code as in panel B. Residues are colored according to the Kyte-Doolittle hydrophobicity scale (*57*), with polar residues colored in blue, intermediate residues in black and hydrophobic residues colored in red. Alignment was performed using the Smith-Waterman algorithm (*58*).
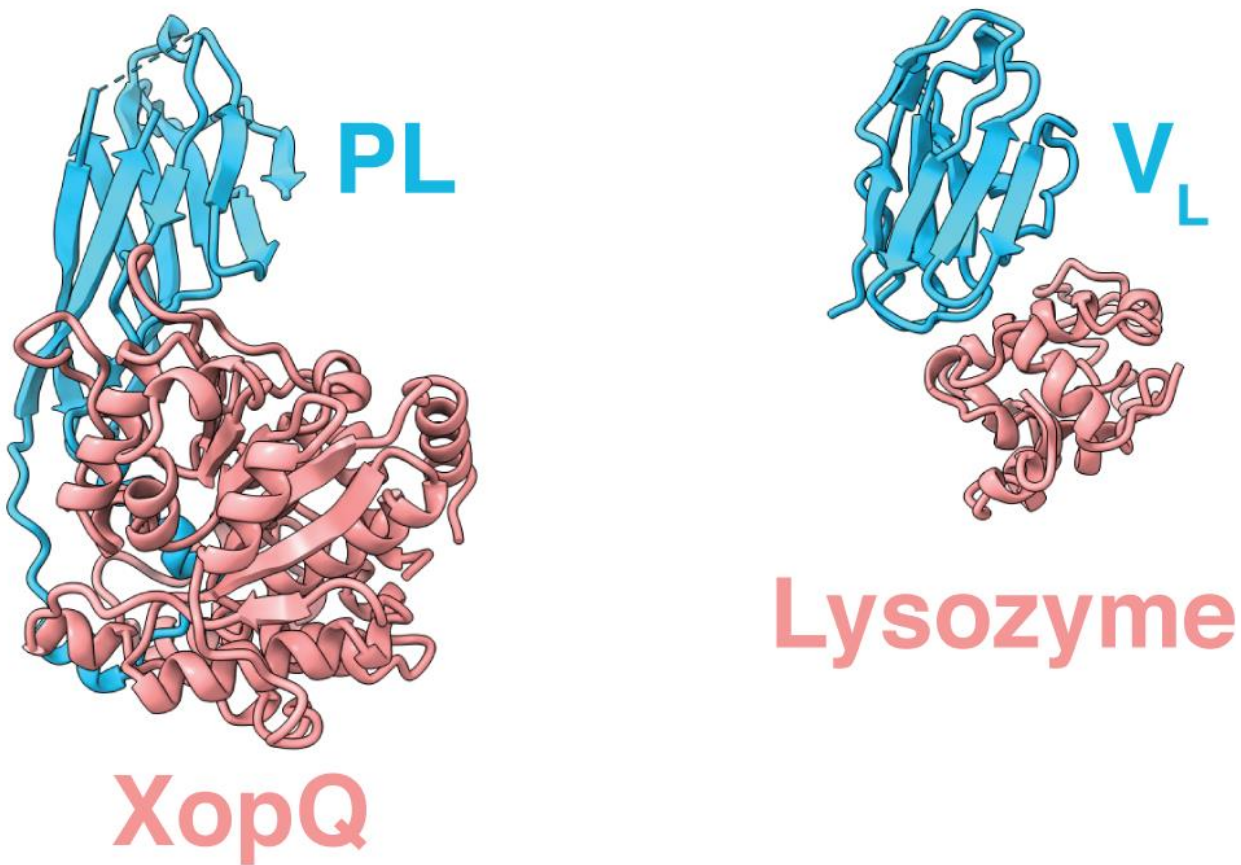
Fig. S6.

Comparison between the C-JID domain of ROQ1 recognizing XopQ (left) and the light-chain variable fragment (V_L) of an antibody recognizing lysozyme (PDB: 3HFM) (right). Loops emerging from the β-sandwich of either the C-JID or V_L (light blue) interact with the substrate (salmon).
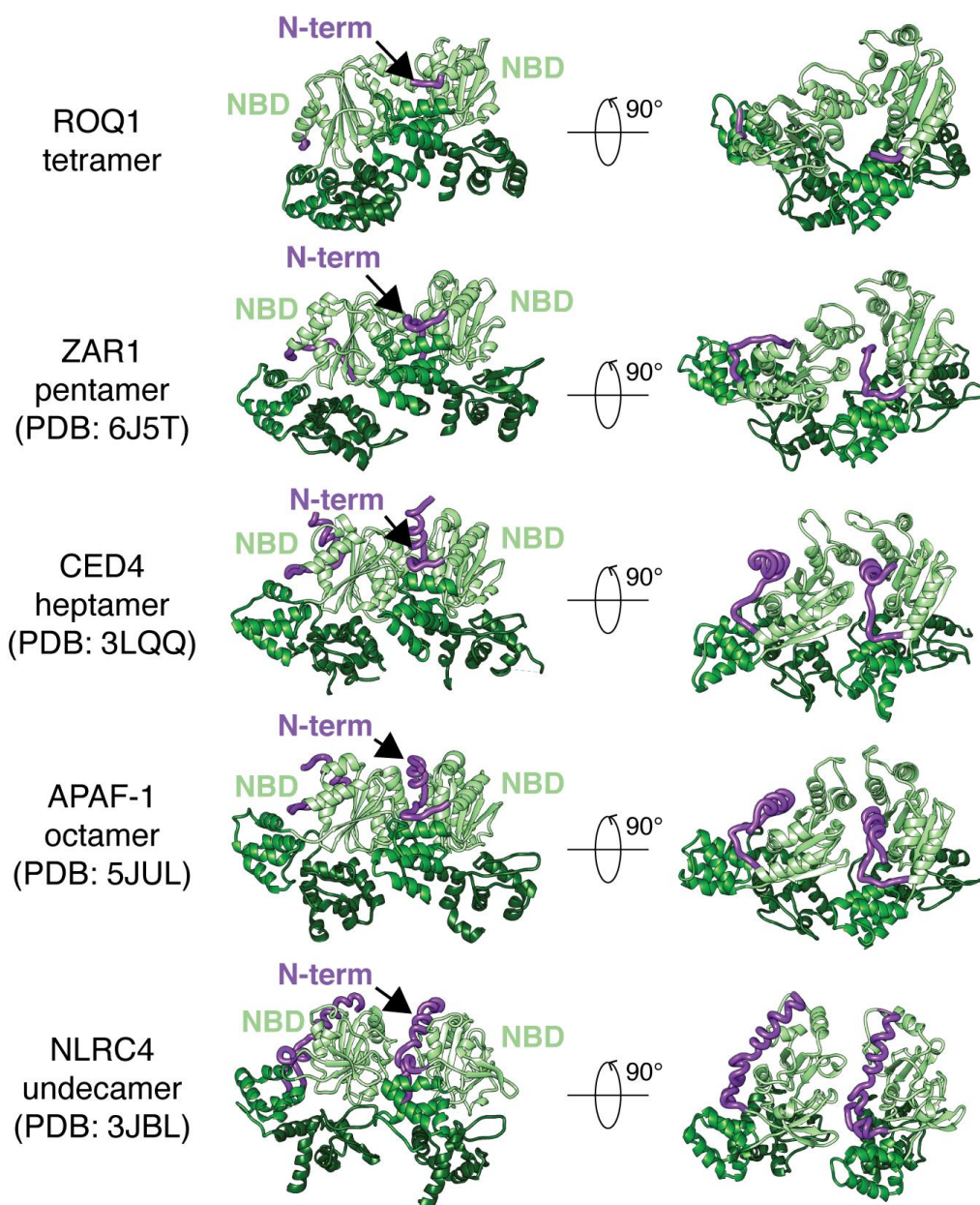
Fig. S7.

Structure of the NBD N-terminal linker (purple) in activated NLRs with increasing oligomeric states. The NBD-HD1-WHD of two neighboring protomers is shown (following the color scheme of ROQ1), with the N-terminal linker of the NBD wedged between them.
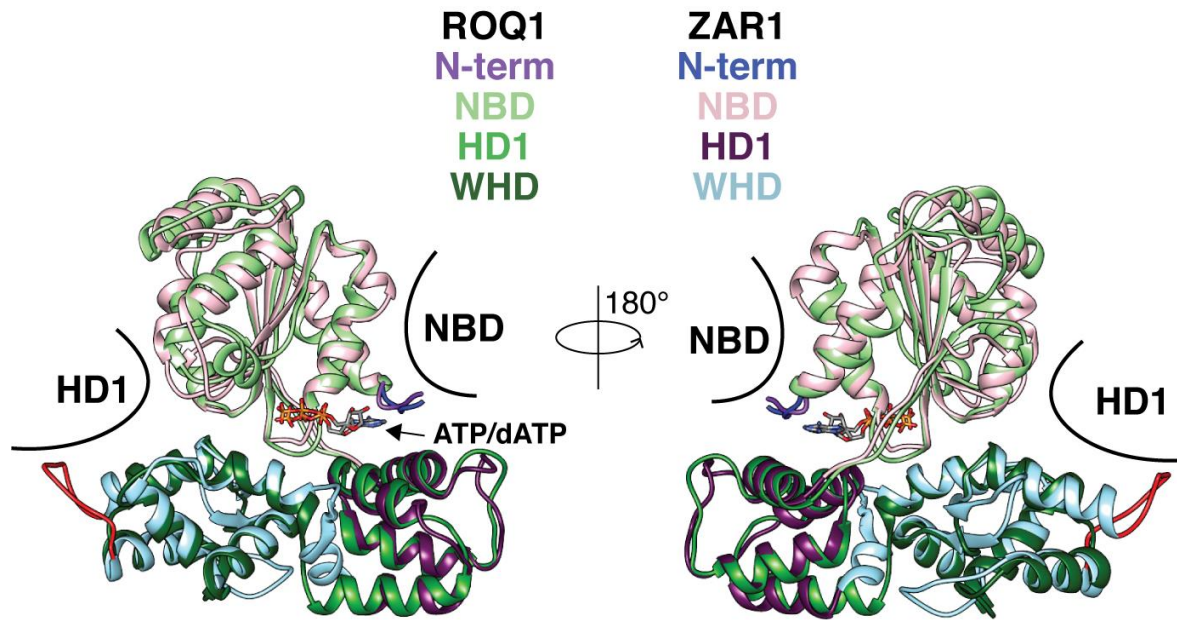
Fig. S8.

Structural comparison between the NB-ARC domain of ROQ1 and ZAR1 in the oligomerized state. The NBD and HD1 of neighboring subunits are represented in black. The NBD and HD1 closely align to each other, whereas we find differences in the loops of the WHD, with one of them extending to make contacts with the neighboring HD1 (red). This loop compensates for the increased distance between the WHD and HD1 in the ZAR1 pentamer relative to the ROQ1 tetramer.
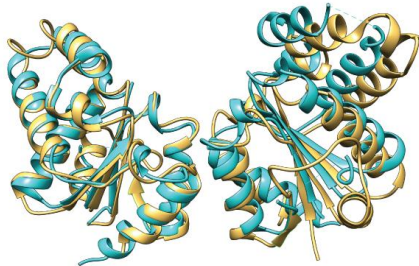
ROQ1 TIR domain

RPP1 TIR doma
(PDB: 5TEB)
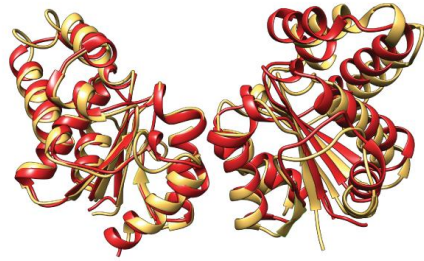
RPV1 TIR doma
(PDB: 5KU7)
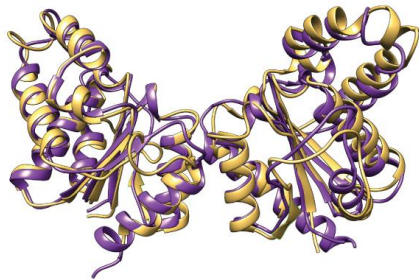
SNC1TIR doma
(PDB: 5TEC)
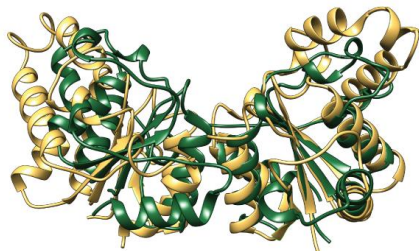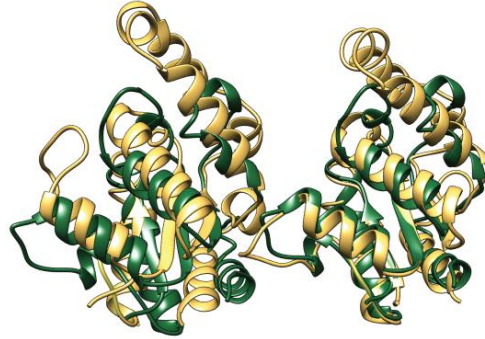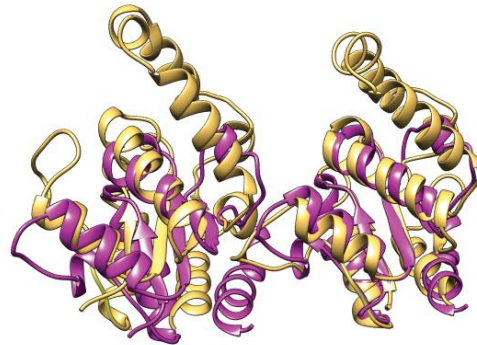
SARM1 TIR domain
(PDB: 6O0R)

Fig. S9.

Structural comparison between the ROQ1 TIR AE interface and the AE interface found in the

crystal lattice of other TIR domains.

ROQ1 TIR domain

SARM1 TIR domain (PDB: 6O0R)

TRR-2 TIR domain (PDB: 4W8G)
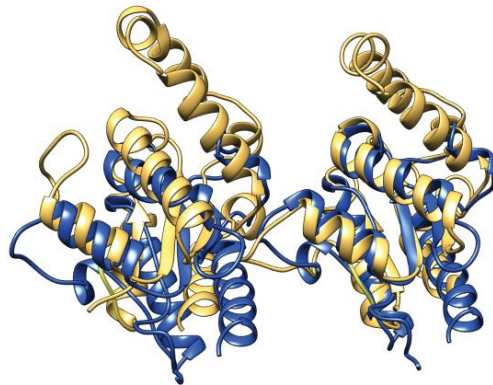
MAL TIR domain (PDB: 5UZB)

Fig. S10.

Structural comparison between the ROQ1 TIR BE interface and the BE interface found in the

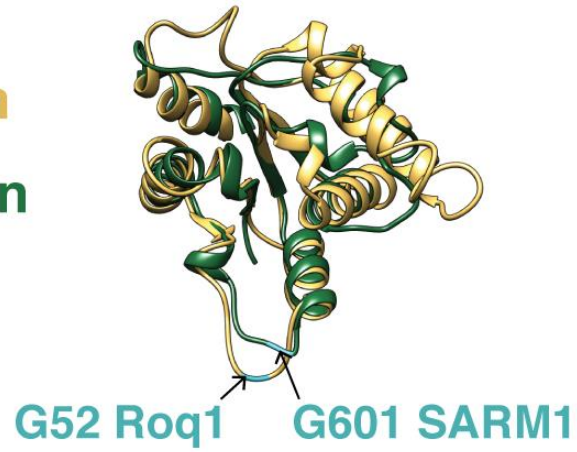crystal lattice of metazoan TIR domains.

Fig. S11.

Position of the BB-loop glycine in both ROQ1 and SARM1 TIR domains. Glycines are represented in cyan.
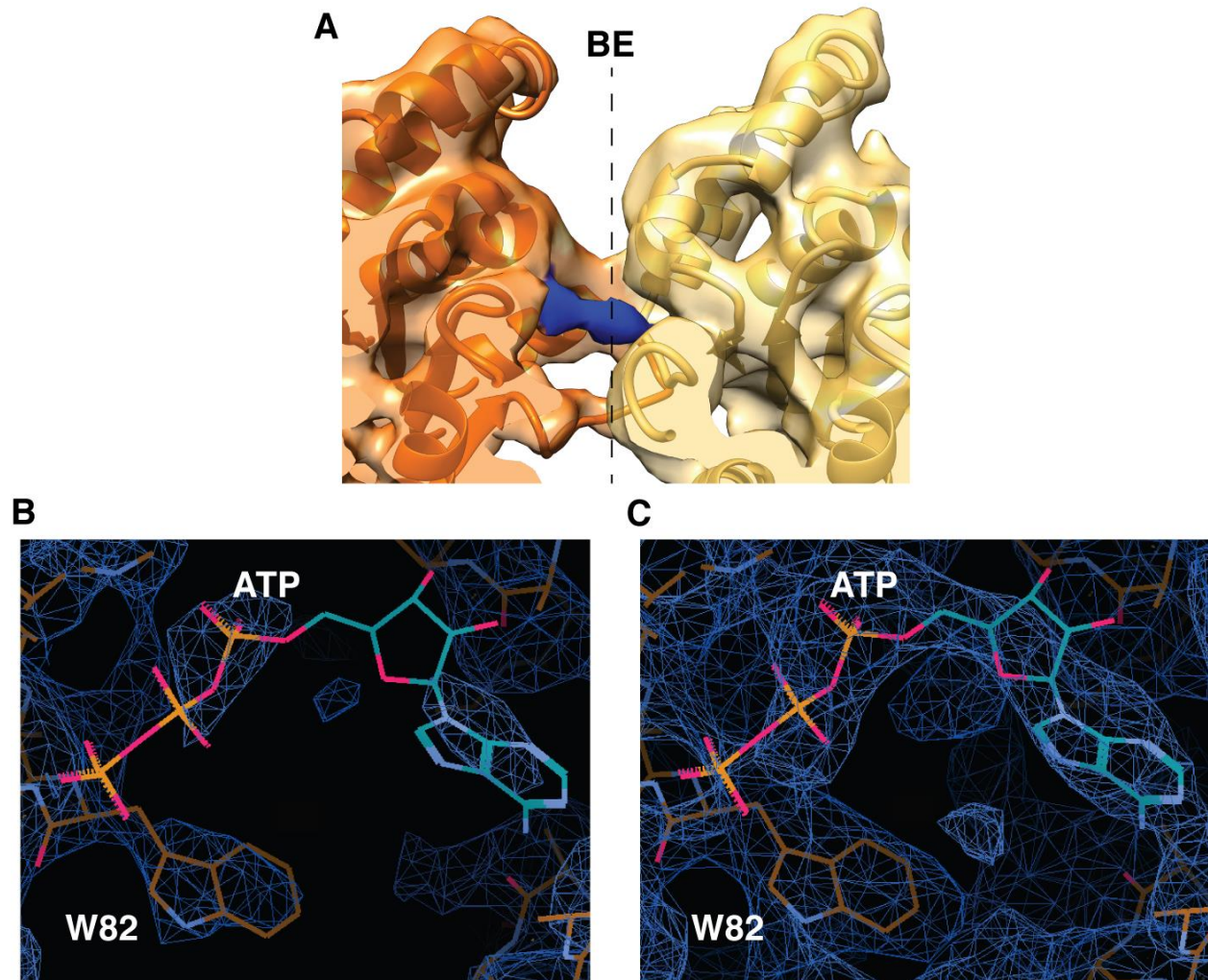
Fig. S12.

A small unidentified density is observed above the TIR domain active site. (A) Two TIR domains at the BE-interface with the unidentified density (blue) in between them. The BB-loop of the TIR domain on the left (orange) is in the engaged state, leaving the NADase active site open. A gaussian filter was applied to the map (width 1.5 Å) to reduce noise. (B,C) An ATP molecule was placed within the unidentified density shown at different contour levels. The nearby tryptophan (W82) density can be used to compare signal strength. While density for W82 is clearly visible at low threshold, density for a hypothetical ATP is very weak. At a higher

threshold, for which there is density that could account for the base, ribose, α-phosphate and part of the β-phosphate of ATP, the density corresponding to W82 is overblown and noise is visible.
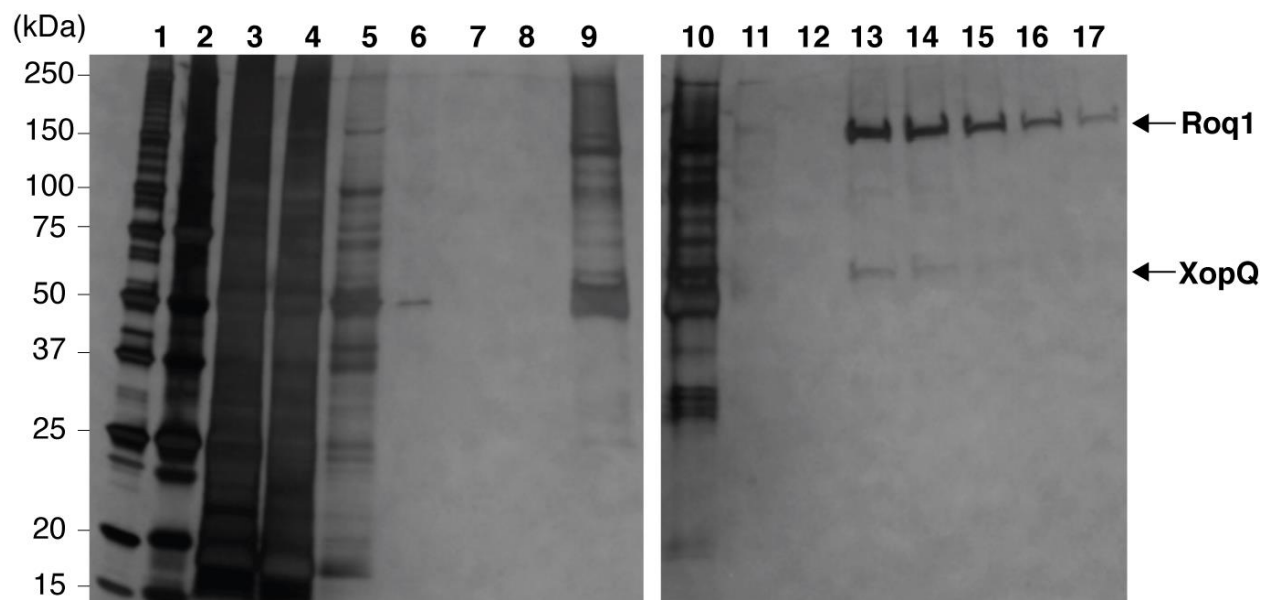
1: 0.5 μL Ladder (Bio-Rad Precision Plus Protein Unstained Standards)
2: 2.5 μL Ladder
3: Lysed cells
4: Flowthrough after binding Roq1-Flag to ANTI-FLAG M2 affinity gel (Sigma-Aldrich)
5-8: Successive washes of ANTI-FLAG M2 affinity gel
9: Elution from ANTI-FLAG M2 affinity gel
10: Flowthrough after binding StrepII-XopQ to Strep-Tactin Superflow Plus resin (Qiagen)
11-12: Successive washes of Strep-Tactin Superflow Plus resin
13-17: Successive elutions from Strep-Tactin Superflow Plus resin (10 μL loaded)

Fig. S13.

Purification of the ROQ1-XopQ complex. Samples were analyzed by SDS-PAGE and silver

stained.

Data Collection

Microscope	Krios
Voltage (kV)	300
Detector	K3
Magnification	80,879x
Energy filter slit (eV)	25
Movies	11,134
Pixel size (Å)	0.9386
Defocus range (µm)	-0.9 to -2.5
Exposure (e⁻/Å²)	50
Exposure rate (e⁻/Å²/frame)	1
Automation software	SerialEM

Reconstruction

Region	Initial reconstruction	LRR-PL-XopQ	TIR domains
Software	RELION	RELION	RELION
Particles (initial)	1,254,987	1,254,987	1,254,987
Particles (final)	15,263	15,263	5,466
Box size (pixels)	480	480	480
Accuracy rotations (°)	0.84	1.28	1.94
Accuracy translations (Å)	0.63	0.98	1.2
Map resolution (Å) FSC = 0.143/0.5	3.8/4.4	3.8/4.4	4.6/8.3
Map sharpening B-factor (Å²)	-82	-67	-97
Local resolution range (Å)	3.4-9.3	3.8-9.7	5.3-24.6

Coordinate Refinement

Software	PHENIX	PHENIX	PHENIX
Resolution Cutoff	3.6	3.8	6
FSC model vs. map = 0.5 (Å)	3.6	3.9	7.7
Model vs. map CC (global/local)	0.80/0.82	0.78/0.78	0.44/0.43

Model

Number of residues

Protein	1748	1079	664
Ligands	8 (4 ATP & 4 Mg²⁺)	1 (Ca²⁺)	None

B-factor (Å²)

Protein	39	65	194
Ligand	31	47	N/A

R.m.s deviations

Bonds lenghts (Å)	0.003	0.003	0.001
Bond angles (°)	0.74	0.772	0.417

Validation

Molprobity score	1.97	2.11	1.52
Molprobity clashscore	9.27	11.55	2.96
Rotamer outliers (%)	0	0.21	0
Cβ deviations (%)	0	0	0

Ramachandran plot

Favored (%)	92.18	90.72	93.29
Allowed (%)	7.82	9.28	6.71
Outliers (%)	0	0	0
CaBLAM outliers (%)	7.16	5.69	2.47
EM ringer score	1.74	1.46	N/A (Cα only)

Deposition

PDB	7JLV	7JLU	7JLX
EMDB	22381	22380	22383

Table S1.

Cryo-EM data collection, data processing, model refinement and validation statistics.

ROQ1
TIR
NBD
HD1
WHD
LRR
C-JID
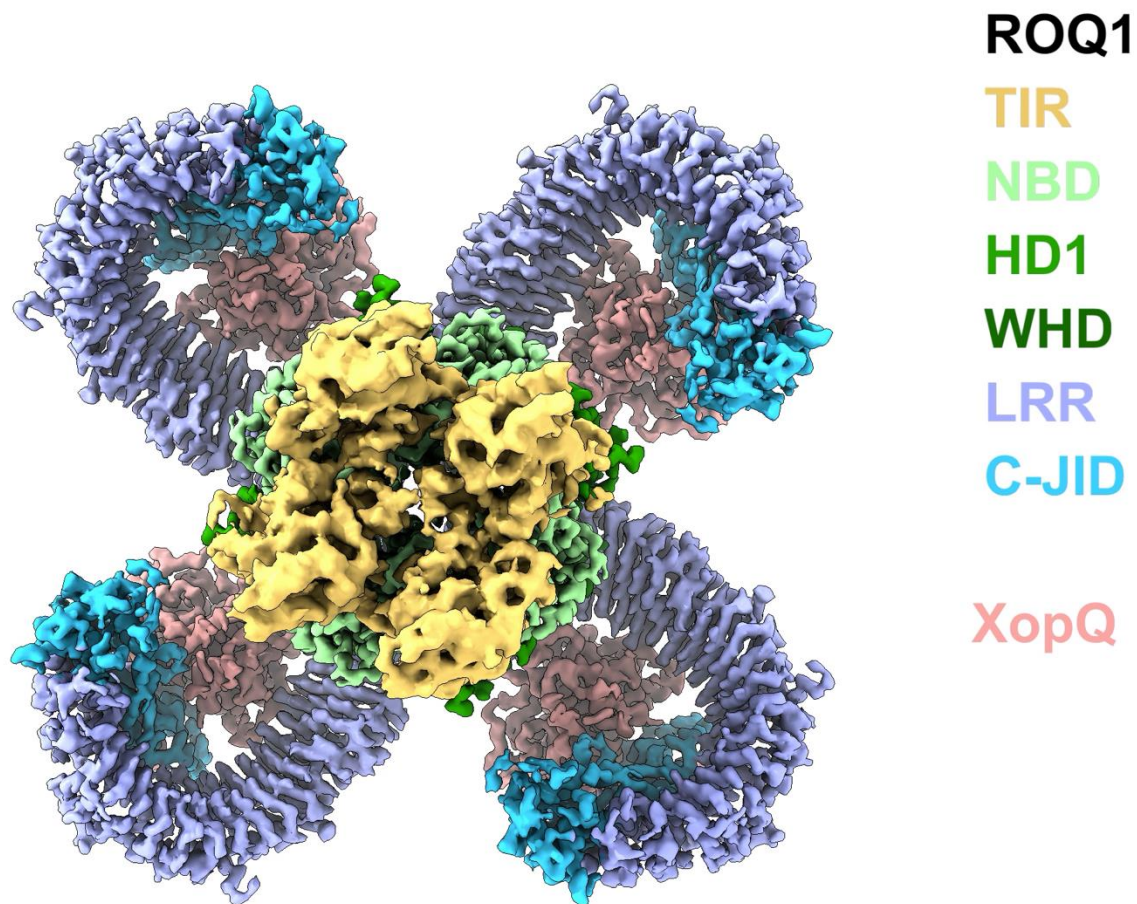
XopQ

Movie S1.

Cryo-EM density map and atomic model of the ROQ1-XopQ complex with colors corresponding
to the different protein domains (as in Fig. 1). Regions of interest are zoomed in to highlight the
different features of the structure.

References and Notes

1. J. L. Dangl, D. M. Horvath, B. J. Staskawicz, Pivoting the plant immune system from dissection to deployment. *Science* **341**, 746–751 (2013). doi:10.1126/science.1236011 Medline

2. J. Wang, J. Chai, Structural insights into the plant immune receptors PRRs and NLRs. *Plant Physiol.* **182**, 1566–1581 (2020). [doi:10.1104/pp.19.01252](doi:10.1104/pp.19.01252) Medline

3. J. Tamborski, K. V. Krasileva, Evolution of plant NLRs: From natural history to precise modifications. *Annu. Rev. Plant Biol.* **71**, 355–378 (2020). doi:10.1146/annurev-arplant-081519-035901 Medline

4. J. M. Feehan, B. Castel, A. R. Bentham, J. D. G. Jones, Plant NLRs get by with a little help from their friends. *Curr. Opin. Plant Biol.* **56**, 99–108 (2020). [doi:10.1016/j.pbi.2020.04.006](doi:10.1016/j.pbi.2020.04.006) Medline

5. L. M. Jubic, S. Saile, O. J. Furzer, F. El Kasmi, J. L. Dangl, Help wanted: Helper NLRs and plant immune responses. *Curr. Opin. Plant Biol.* **50**, 82–94 (2019). [doi:10.1016/j.pbi.2019.03.013](doi:10.1016/j.pbi.2019.03.013) Medline

6. J. D. G. Jones, R. E. Vance, J. L. Dangl, Intracellular innate immune surveillance devices in plants and animals. *Science* **354**, aaf6395 (2016). doi:10.1126/science.aaf6395 Medline

7. J. Wang, J. Wang, M. Hu, S. Wu, J. Qi, G. Wang, Z. Han, Y. Qi, N. Gao, H.-W. Wang, J.-M. Zhou, J. Chai, Ligand-triggered allosteric ADP release primes a plant NLR complex. *Science* **364**, eaav5868 (2019). doi:10.1126/science.aav5868 Medline

8. J. Wang, M. Hu, J. Wang, J. Qi, Z. Han, G. Wang, Y. Qi, H. W. Wang, J. M. Zhou, J. Chai, Reconstitution and structure of a plant NLR resistosome conferring immunity. *Science* **364**, eaav5870 (2019). doi:10.1126/science.aav5870 Medline

9. L. Wan, K. Essuman, R. G. Anderson, Y. Sasaki, F. Monteiro, E.-H. Chung, E. Osborne Nishimura, A. DiAntonio, J. Milbrandt, J. L. Dangl, M. T. Nishimura, TIR domains of plant immune receptors are NAD^+-cleaving enzymes that promote cell death. *Science* **365**, 799–803 (2019). doi:10.1126/science.aax1771 Medline

10. S. Horsefield, H. Burdett, X. Zhang, M. K. Manik, Y. Shi, J. Chen, T. Qi, J. Gilley, J.-S. Lai, M. X. Rank, L. W. Casey, W. Gu, D. J. Ericsson, G. Foley, R. O. Hughes, T. Bosanac, M. von Itzstein, J. P. Rathjen, J. D. Nanson, M. Boden, I. B. Dry, S. J. Williams, B. J. Staskawicz, M. P. Coleman, T. Ve, P. N. Dodds, B. Kobe, NAD^+ cleavage activity by animal and plant TIR domains in cell death pathways. *Science* **365**, 793–799 (2019). doi:10.1126/science.aax1911 Medline

11. A. Schultink, T. Qi, A. Lee, A. D. Steinbrenner, B. Staskawicz, Roq1 mediates recognition of the Xanthomonas and Pseudomonas effector proteins XopQ and HopQ1. *Plant J.* **92**, 787–795 (2017). [doi:10.1111/tpj.13715](doi:10.1111/tpj.13715) Medline

12. T. Qi, K. Seong, D. P. T. Thomazella, J. R. Kim, J. Pham, E. Seo, M.-J. Cho, A. Schultink, B. J. Staskawicz, NRG1 functions downstream of EDS1 to regulate TIR-NLR-mediated plant immunity in *Nicotiana benthamiana*. *Proc. Natl. Acad. Sci. U.S.A.* **115**, E10979–E10987 (2018). doi:10.1073/pnas.1814856115 Medline

13. D. Lapin, D. D. Bhandari, J. E. Parker, Origins and immunity networking functions of EDS1 family proteins. *Annu. Rev. Phytopathol.* **58**, 253–276 (2020). doi:10.1146/annurev-phyto-010820-012840 Medline

14. S. Yu, I. Hwang, S. Rhee, The crystal structure of type III effector protein XopQ from Xanthomonas oryzae complexed with adenosine diphosphate ribose. *Proteins* **82**, 2910–2914 (2014). doi:10.1002/prot.24656 Medline

15. L. Liu, I. Botos, Y. Wang, J. N. Leonard, J. Shiloach, D. M. Segal, D. R. Davies, Structural basis of toll-like receptor 3 signaling with double-stranded RNA. *Science* **320**, 379–381 (2008). doi:10.1126/science.1155406 Medline

16. C. Van Ghelder, D. Esmenjaud, TNL genes in peach: Insights into the post-LRR domain. *BMC Genomics* **17**, 317 (2016). doi:10.1186/s12864-016-2635-0 Medline

17. I. Sillitoe, N. Dawson, T. E. Lewis, S. Das, J. G. Lees, P. Ashford, A. Tolulope, H. M. Scholes, I. Senatorov, A. Bujan, F. Ceballos Rodriguez-Conde, B. Dowling, J. Thornton, C. A. Orengo, CATH: Expanding the horizons of structure-based functional annotations for genome sequences. *Nucleic Acids Res.* **47** (D1), D280–D284 (2019). doi:10.1093/nar/gky1097 Medline

18. S. Ma, D. Lapin, L. Liu, Y. Sun, W. Song, X. Zhang, E. Logemann, D. Yu, J. Wang, J. Jirschitzka, Z. Han, P. Schulze-Lefert, J. E. Parker, J. Chai, Direct pathogen-induced assembly of an NLR immune receptor complex to form a holoenzyme. *Science* 10.1126/science.abe3069 (2020). doi:10.1126/science.abe3069

19. W. Li, Y.-H. Chiang, G. Coaker, The HopQ1 effector's nucleoside hydrolase-like domain is required for bacterial virulence in arabidopsis and tomato, but not host recognition in tobacco. *PLOS ONE* **8**, e59684 (2013). doi:10.1371/journal.pone.0059684 Medline

20. N. Adlung, U. Bonas, Dissecting virulence function from recognition: Cell death suppression in Nicotiana benthamiana by XopQ/HopQ1-family effectors relies on EDS1-dependent immunity. *Plant J.* **91**, 430–442 (2017). doi:10.1111/tpj.13578 Medline

21. Y. Xiong, Z. Han, J. Chai, Resistosome and inflammasome: Platforms mediating innate immunity. *Curr. Opin. Plant Biol.* **56**, 47–55 (2020). doi:10.1016/j.pbi.2020.03.010 Medline

22. J. F. C. Steele, R. K. Hughes, M. J. Banfield, Structural and biochemical studies of an NB-ARC domain from a plant NLR immune receptor. *PLOS ONE* **14**, e0221226 (2019). doi:10.1371/journal.pone.0221226 Medline

23. Z. Hu, C. Yan, P. Liu, Z. Huang, R. Ma, C. Zhang, R. Wang, Y. Zhang, F. Martinon, D. Miao, H. Deng, J. Wang, J. Chang, J. Chai, Crystal structure of NLRC4 reveals its autoinhibition mechanism. *Science* **341**, 172–175 (2013). doi:10.1126/science.1236381 Medline

24. Y. Pang, X. C. Bai, C. Yan, Q. Hao, Z. Chen, J. W. Wang, S. H. W. Scheres, Y. Shi, Structure of the apoptosome: Mechanistic insights into activation of an initiator caspase from Drosophila. *Genes Dev.* **29**, 277–287 (2015). doi:10.1101/gad.255877.114 Medline

25. S. Qi, Y. Pang, Q. Hu, Q. Liu, H. Li, Y. Zhou, T. He, Q. Liang, Y. Liu, X. Yuan, G. Luo, H. Li, J. Wang, N. Yan, Y. Shi, Crystal structure of the *Caenorhabditis elegans* apoptosome

reveals an octameric assembly of CED-4. *Cell* **141**, 446–457 (2010). doi:10.1016/j.cell.2010.03.017 Medline

26. J. L. Tenthorey, N. Haloupek, J. R. López-Blanco, P. Grob, E. Adamson, E. Hartenian, N. A. Lind, N. M. Bourgeois, P. Chacón, E. Nogales, R. E. Vance, The structural basis of flagellin detection by NAIP5: A strategy to limit pathogen immune evasion. *Science* **358**, 888–893 (2017). doi:10.1126/science.aao1140 Medline

27. L. Zhang, S. Chen, J. Ruan, J. Wu, A. B. Tong, Q. Yin, Y. Li, L. David, A. Lu, W. L. Wang, C. Marks, Q. Ouyang, X. Zhang, Y. Mao, H. Wu, Cryo-EM structure of the activated NAIP2-NLRC4 inflammasome reveals nucleated polymerization. *Science* **350**, 404–409 (2015). doi:10.1126/science.aac5789 Medline

28. V. Bonardi, K. Cherkis, M. T. Nishimura, J. L. Dangl, A new eye on NLR proteins: Focused on clarity or diffused by complexity? *Curr. Opin. Immunol.* **24**, 41–50 (2012). doi:10.1016/j.coi.2011.12.006 Medline

29. X. Yang, F. Yang, W. Wang, G. Lin, Z. Hu, Z. Han, Y. Qi, L. Zhang, J. Wang, S.-F. Sui, J. Chai, Structural basis for specific flagellin recognition by the NLR protein NAIP5. *Cell Res.* **28**, 35–47 (2018). doi:10.1038/cr.2017.148 Medline

30. E. F. Halff, C. A. Diebolder, M. Versteeg, A. Schouten, T. H. C. Brondijk, E. G. Huizinga, Formation and structure of a NAIP5-NLRC4 inflammasome induced by direct interactions with conserved N- and C-terminal regions of flagellin. *J. Biol. Chem.* **287**, 38460–38472 (2012). doi:10.1074/jbc.M112.393512 Medline

31. A. M. Bayless, M. T. Nishimura, Enzymatic functions for Toll/interleukin-1 receptor domain proteins in the plant immune system. *Front. Genet.* **11**, 539 (2020). doi:10.3389/fgene.2020.00539 Medline

32. X. Zhang, M. Bernoux, A. R. Bentham, T. E. Newman, T. Ve, L. W. Casey, T. M. Raaymakers, J. Hu, T. I. Croll, K. J. Schreiber, B. J. Staskawicz, P. A. Anderson, K. H. Sohn, S. J. Williams, P. N. Dodds, B. Kobe, Multiple functional self-association interfaces in plant TIR domains. *Proc. Natl. Acad. Sci. U.S.A.* **114**, E2046–E2052 (2017). doi:10.1073/pnas.1621248114 Medline

33. S. J. Williams, K. H. Sohn, L. Wan, M. Bernoux, P. F. Sarris, C. Segonzac, T. Ve, Y. Ma, S. B. Saucet, D. J. Ericsson, L. W. Casey, T. Lonhienne, D. J. Winzor, X. Zhang, A. Coerdt, J. E. Parker, P. N. Dodds, B. Kobe, J. D. G. Jones, Structural basis for assembly and function of a heterodimeric plant immune receptor. *Science* **344**, 299–303 (2014). doi:10.1126/science.1247357 Medline

34. K.-G. Hyun, Y. Lee, J. Yoon, H. Yi, J.-J. Song, Crystal structure of Arabidopsis thaliana SNC1 TIR domain. *Biochem. Biophys. Res. Commun.* **481**, 146–152 (2016). doi:10.1016/j.bbrc.2016.11.004 Medline

35. M. Bernoux, T. Ve, S. Williams, C. Warren, D. Hatters, E. Valkov, X. Zhang, J. G. Ellis, B. Kobe, P. N. Dodds, Structural and functional analysis of a plant resistance protein TIR domain reveals interfaces for self-association, signaling, and autoregulation. *Cell Host Microbe* **9**, 200–211 (2011). doi:10.1016/j.chom.2011.02.009 Medline

36. S. J. Williams, L. Yin, G. Foley, L. W. Casey, M. A. Outram, D. J. Ericsson, J. Lu, M. Boden, I. B. Dry, B. Kobe, Structure and function of the TIR domain from the grape NLR

protein RPV1. *Front. Plant Sci.* **7**, 1850 (2016). Medline

37. Y. Xu, X. Tao, B. Shen, T. Horng, R. Medzhitov, J. L. Manley, L. Tong, Structural basis for signal transduction by the Toll/interleukin-1 receptor domains. *Nature* **408**, 111–115 (2000). doi:10.1038/35040600 Medline

38. S. Nimma, T. Ve, S. J. Williams, B. Kobe, Towards the structure of the TIR-domain signalosome. *Curr. Opin. Struct. Biol.* **43**, 122–130 (2017). doi:10.1016/j.sbi.2016.12.014 Medline

39. L. Vyncke, C. Bovijn, E. Pauwels, T. Van Acker, E. Ruyssinck, E. Burg, J. Tavernier, F. Peelman, Reconstructing the TIR side of the myddosome: A paradigm for TIR-TIR interactions. *Structure* **24**, 437–447 (2016). doi:10.1016/j.str.2015.12.018 Medline

40. T. Ve, P. R. Vajjhala, A. Hedger, T. Croll, F. DiMaio, S. Horsefield, X. Yu, P. Lavrencic, Z. Hassan, G. P. Morgan, A. Mansell, M. Mobli, A. O'Carroll, B. Chauvin, Y. Gambin, E. Sierecki, M. J. Landsberg, K. J. Stacey, E. H. Egelman, B. Kobe, Structural basis of TIR-domain-assembly formation in MAL- and MyD88-dependent TLR4 signaling. *Nat. Struct. Mol. Biol.* **24**, 743–751 (2017). doi:10.1038/nsmb.3444 Medline

41. K. Essuman, D. W. Summers, Y. Sasaki, X. Mao, A. K. Y. Yim, A. DiAntonio, J. Milbrandt, TIR domain proteins are an ancient family of NAD$^+$-consuming enzymes. *Curr. Biol.* **28**, 421–430.e4 (2018). doi:10.1016/j.cub.2017.12.024 Medline

42. Y. Wu, J. Kuzma, E. Maréchal, R. Graeff, H. C. Lee, R. Foster, N. H. Chua, Abscisic acid signaling through cyclic ADP-ribose in plants. *Science* **278**, 2126–2130 (1997). doi:10.1126/science.278.5346.2126 Medline

43. S. H. W. Scheres, RELION: Implementation of a Bayesian approach to cryo-EM structure determination. *J. Struct. Biol.* **180**, 519–530 (2012). doi:10.1016/j.jsb.2012.09.006 Medline

44. K. Zhang, Gctf: Real-time CTF determination and correction. *J. Struct. Biol.* **193**, 1–12 (2016). doi:10.1016/j.jsb.2015.11.003 Medline

45. S. Q. Zheng, E. Palovcak, J.-P. Armache, K. A. Verba, Y. Cheng, D. A. Agard, MotionCor2: Anisotropic correction of beam-induced motion for improved cryo-electron microscopy. *Nat. Methods* **14**, 331–332 (2017). doi:10.1038/nmeth.4193 Medline

46. P. Emsley, K. Cowtan, Coot: Model-building tools for molecular graphics. *Acta Crystallogr. D Biol. Crystallogr.* **60**, 2126–2132 (2004). doi:10.1107/S0907444904019158 Medline

47. P. D. Adams, R. W. Grosse-Kunstleve, L. W. Hung, T. R. Ioerger, A. J. McCoy, N. W. Moriarty, R. J. Read, J. C. Sacchettini, N. K. Sauter, T. C. Terwilliger, PHENIX: Building new software for automated crystallographic structure determination. *Acta Crystallogr. D Biol. Crystallogr.* **58**, 1948–1954 (2002). doi:10.1107/S0907444902016657 Medline

48. P. V. Afonine, B. P. Klaholz, N. W. Moriarty, B. K. Poon, O. V. Sobolev, T. C. Terwilliger, P. D. Adams, A. Urzhumtsev, New tools for the analysis and validation of cryo-EM maps and atomic models. *Acta Crystallogr. D Struct. Biol.* **74**, 814–840 (2018). doi:10.1107/S2059798318009324 Medline

49. H. Ashkenazy, S. Abadi, E. Martz, O. Chay, I. Mayrose, T. Pupko, N. Ben-Tal, ConSurf

2016: An improved methodology to estimate and visualize evolutionary conservation in macromolecules. *Nucleic Acids Res.* **44** (W1), W344–W350 (2016). doi:10.1093/nar/gkw408 Medline

50. J. Zivanov, T. Nakane, B. O. Forsberg, D. Kimanius, W. J. Hagen, E. Lindahl, S. H. Scheres, New tools for automated high-resolution cryo-EM structure determination in RELION-3. *eLife* **7**, e42166 (2018). doi:10.7554/eLife.42166 Medline

51. A. Punjani, J. L. Rubinstein, D. J. Fleet, M. A. Brubaker, cryoSPARC: Algorithms for rapid unsupervised cryo-EM structure determination. *Nat. Methods* **14**, 290–296 (2017). doi:10.1038/nmeth.4169 Medline

52. A. Waterhouse, M. Bertoni, S. Bienert, G. Studer, G. Tauriello, R. Gumienny, F. T. Heer, T. A. P. de Beer, C. Rempfer, L. Bordoli, R. Lepore, T. Schwede, SWISS-MODEL: Homology modelling of protein structures and complexes. *Nucleic Acids Res.* **46** (W1), W296–W303 (2018). doi:10.1093/nar/gky427 Medline

53. L. A. Kelley, S. Mezulis, C. M. Yates, M. N. Wass, M. J. E. Sternberg, The Phyre2 web portal for protein modeling, prediction and analysis. *Nat. Protoc.* **10**, 845–858 (2015). doi:10.1038/nprot.2015.053 Medline

54. E. F. Pettersen, T. D. Goddard, C. C. Huang, G. S. Couch, D. M. Greenblatt, E. C. Meng, T. E. Ferrin, UCSF Chimera—A visualization system for exploratory research and analysis. *J. Comput. Chem.* **25**, 1605–1612 (2004). doi:10.1002/jcc.20084 Medline

55. C. J. Williams, J. J. Headd, N. W. Moriarty, M. G. Prisant, L. L. Videau, L. N. Deis, V. Verma, D. A. Keedy, B. J. Hintze, V. B. Chen, S. Jain, S. M. Lewis, W. B. Arendall 3rd, J. Snoeyink, P. D. Adams, S. C. Lovell, J. S. Richardson, D. C. Richardson, MolProbity: More and better reference data for improved all-atom structure validation. *Protein Sci.* **27**, 293–315 (2018). doi:10.1002/pro.3330 Medline

56. K. Katoh, D. M. Standley, MAFFT multiple sequence alignment software version 7: Improvements in performance and usability. *Mol. Biol. Evol.* **30**, 772–780 (2013). doi:10.1093/molbev/mst010 Medline

57. J. Kyte, R. F. Doolittle, A simple method for displaying the hydropathic character of a protein. *J. Mol. Biol.* **157**, 105–132 (1982). doi:10.1016/0022-2836(82)90515-0 Medline

58. T. F. Smith, M. S. Waterman, Identification of common molecular subsequences. *J. Mol. Biol.* **147**, 195–197 (1981). doi:10.1016/0022-2836(81)90087-5 Medline